J. Fluid Mech. (1998), *vol.* 363, *pp.* 253–280. Printed in the United Kingdom

The effects of wall inertia on flow in a two-dimensional collapsible channel

By X. Y. LUO[1] AND T. J. PEDLEY[2]

[1]Department of Engineering, Queen Mary & Westfield College, The University of London, London E1 4NS, UK

[2]Department of Applied Mathematics and Theoretical Physics, University of Cambridge, Silver Street, Cambrige CB3 9EW, UK

(Received 20 December 1996 and in revised form 3 October 1997)

The effect of wall inertia on the self-excited oscillations in a collapsible channel flow is investigated by solving the full coupled two-dimensional membrane–flow equations. This is the continuation of a previous study in which self-excited oscillations were predicted in an asymmetric channel with a tensioned massless elastic membrane (Luo & Pedley 1996). It is found that a different type of self-excited oscillation, a form of flutter, is superposed on the original large-amplitude, low-frequency oscillations. Unlike the tension-induced oscillations, the flutter has high frequency, and grows with time from a small amplitude until it dominates the original slower mode. The critical value of tension below which oscillations arise (at fixed Reynolds number) is found to increase as the wall inertia is increased. The rate at which energy is (*a*) dissipated in the flow field and (*b*) transferred to the wall during the flutter is discussed, and results at different parameter values are compared with those of a massless membrane. There is also a discussion of whether the onset of flutter, or that of the slower oscillations, is correlated with the appearance of flow limitation, as is thought to be the case in the context of wheezing during forced expiration of air from the lungs.

1. Introduction

There are number of physiological applications that are related to the fluid mechanics of flow in collapsible tubes. Examples are arteries compressed by a sphygmomanometer cuff, intramyocardial coronary blood vessels during systole, pulmonary blood vessels in large intrathoracic airways during forced expiration, the urethra during micturition, and the glottis during phonation (Shapiro 1977; Kamm & Pedley 1989).

Many experiments with model systems of collapsible tubes in the laboratory have revealed a rich variety of self-excited oscillations (Conrad 1969; Brower & Scholten 1975; Bonis & Ribreau 1978; Bertram 1982, 1986; Bertram, Raymond & Pedley 1990, 1991). In these experiments either water or air flow has been studied in a segment of rubber tube. The observations have stimulated several theoretical studies aimed at understanding the possible mechanisms of the oscillations. Many such studies have been based on plausible but *ad hoc* one-dimensional models, which may explain some of the phenomena that have been observed in the experiments (e.g. Reyn 1974; Shapiro 1977; Cancelli & Pedley 1985; Jensen & Pedley 1989; Jensen 1990, 1992; Matsuzaki & Matsumoto 1989; Pedley 1992), but recently there have also been

numerical simulations based on a two-dimensional model, i.e. flow in an asymmetric collapsible channel (Rast 1994; Lowe & Pedley 1995; Lowe, Luo & Rast 1996; Luo & Pedley 1995, 1996). This approach has provided a rational, yet feasible, description of an experimentally realizable system, although it is still some way from the full three-dimensional tube system.

An earlier stage of these studies concentrated on the existence of steady solutions for flow in a channel with part of one wall being a thin membrane, for different values of the longitudinal tension along the membrane, and different values of Reynolds number, Re, and downstream transmural pressure (external minus internal). It was found that there was a critical value of tension, T_c, depending on Re, below which no numerical solution was attainable (Rast 1994; Lowe & Pedley 1995; Luo & Pedley 1995). However, simple one-dimensional analyses suggest that the breakdown was more likely to be numerical than physical. Further study was carried out on the stability of the steady solutions, and the main conclusion was that they give way to a range of self-excited oscillations for values of tension smaller than T_u, where T_u is much larger than T_c and increases with Re (Luo & Pedley 1996).

All these studies were carried out for an elastic wall behaving like a tensioned membrane, without wall inertia. The reason for neglecting the wall inertia was that it comes into the equation as the wall-to-fluid density ratio multiplied by the ratio of membrane thickness to the whole channel width, which is very small if the fluid is water. In this paper, we will extend the previous study by considering the effects of wall inertia, not only to justify the assumption made in the previous study, but also to look at the cases where the wall inertia is not negligible, say if the fluid is air.

The study of flow-induced oscillation in tubes and channels has a long history, with proposed applications in either engineering (Carpenter & Garrad 1986; Carpenter & Morris 1990) or physiology, notably in the context of expiratory wheezing in airways (Gavriely & Grotberg 1988; Gavriely *et al.* 1989; Grotberg & Gavriely 1989; Webster *et al.* 1985). Almost all these studies, however, consisted of linear or nonlinear instability theories for flow in a long, *parallel-sided* channel, so in the basic state the steady flow is unidirectional and the elastic walls are planar. This should be contrasted with the present case, in which the steady flow, from which the oscillations grow, involves a large deformation of the wall and separation of the flow (Luo & Pedley 1995, 1996). In fact, one of the principal questions of interest in the context of forced expiration from the lungs is whether there is a causal relationship between wheezing and 'flow limitation', i.e. the phenomenon that increasing a large expiratory driving pressure does not lead to an increase in flow rate on account of airway collapse. Gavriely *et al.* (1989) and Grotberg & Gavriely (1989) sought to analyse the phenomenon by applying their flutter theory, developed for a parallel-sided channel, to a channel of slowly varying width, representing the narrowest part of the collapsed airway. Their results showed an encouraging agreement with a model experiment (indicating that flow limitation is necessary but not sufficient for the onset of flutter), but as far as we know the present study is the first time that collapse and flutter will have been examined together, self-consistently, in the same model problem.

The two-dimensional model is briefly reviewed in §2, and the numerical methods are given in §3, which focuses mainly on how to incorporate the wall inertia into the numerical code. Computational accuracy is discussed at the end of the section. Results are compared with those from the massless wall, obtained previously (Luo & Pedley 1996), in §4, followed by a full discussion and comparison with the flutter theories in §5.

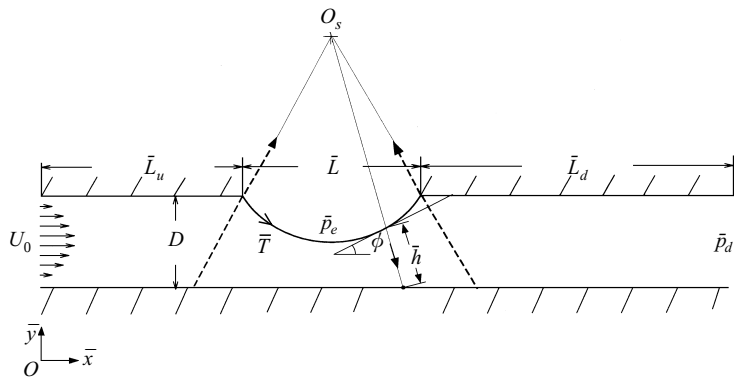

FIGURE 1. Two-dimensional flow configuration. Steady Poiseuille flow with average velocity U_0 entering upstream; $\bar{p}_d = 0$ is pressure at the downstream end of the channel, $\bar{p}_e$ is the external pressure and $\bar{T}$ is the tension in the membrane. For explanation of other symbols, see text.

2. The mathematical model

2.1. *Assumptions*

The flow configuration is shown in figure 1. The rigid channel has width D; one part of the upper wall is replaced by an elastic membrane subjected to an external pressure $\bar{p}_e$. Steady Poiseuille flow with average velocity U_0 is assumed at the entrance; the fluid pressure at the downstream end is zero. The flow is incompressible and laminar, the fluid having density ρ and viscosity μ. The longitudinal tension $\bar{T}$ is taken to be constant, i.e. variations due to the wall shear stress or the overall change of the membrane length are considered to be small relative to the initial stretching tension.

2.2. *Governing equations*

The dimensionless momentum and continuity equations are, in standard notation,

$$\frac{\partial u_i}{\partial t} + u_j u_{i,j} = -p_{,i} + \frac{1}{Re} u_{i,jj}, \tag{1}$$

$$u_{i,i} = 0, \qquad i = 1, 2, \tag{2}$$

where $Re = U_0 D\rho/\mu$ is the Reynolds number. The dimensionless membrane equation is:

$$m\frac{\partial^2 \eta}{\partial t^2} - \kappa T - \sigma_n + p_e = 0, \tag{3}$$

where m is the ratio of the inertia of the membrane to the inertia of the fluid (see below), η is the dimensionless displacement of the membrane in the normal direction, σ_n is the dimensionless fluid stress acting on the membrane in the normal direction, p_e is the external pressure, T is the longitudinal tension, and κ is the wall curvature which can be expressed as the derivative along the membrane of the angle made by the tangent to the elastic boundary with the x-axis:

$$\kappa = \frac{\partial \phi}{\partial s}. \tag{4}$$

All the variables are non-dimensionalized as

$$\left.\begin{aligned} u_i = \bar{u}_i/U_0 \quad (i=1,2), \quad \sigma = \bar{\sigma}/\rho U_0^2, \quad p = \bar{p}/\rho U_0^2, \\ T = \overline{T}/\rho U_0^2 D, \quad x = \bar{x}/D, \quad y = \bar{y}/D, \\ \eta = \bar{\eta}/D, \quad s = \bar{s}/D, \quad t = \bar{t}U_0/D, \quad m = \frac{\rho_w w}{\rho D}, \end{aligned}\right\} \tag{5}$$

where an overbar denote-dimensional variables. Note that ρ_w and ρ are the densities of the membrane and fluid, respectively, and w denotes the thickness of the membrane which is taken to be much smaller than the channel width D. Therefore, if the fluid density is comparable with the membrane density, say if we use water and rubber, then m should be very small; $m \simeq 0.01$ is a reasonable value for comparison with certain experiments (Sakurai & Ohba 1986; Ohba *et al.* 1984). Increasing m will yield results more relevant to gas flows than liquid flows, or to thicker membranes. However, quantitative agreement with tube flow experiments is not to be expected, because in this model all the stiffness of the collapsible segment comes from tension in the membrane, not bending of the tube wall which is the major factor in many tubes.

2.3. *Boundary and initial conditions*

The boundary conditions imposed on the flow domain are:

inlet flow:	$u = 6y(1-y),\ v = 0$	at	$x = 0,\ 0 \leqslant y \leqslant 1,$
rigid walls:	$u = v = 0$	at	$y = 0,\ 0 \leqslant x \leqslant L_u + L + L_d,$
		at	$y = 1,\ 0 \leqslant x \leqslant L_u$ and
			$L_u + L \leqslant x \leqslant L_u + L + L_d,$
elastic section:	$u(t) = u_w(t);\ v(t) = v_w(t)$	at	$x = x_w(t),\ y = y_w(t),$
outflow:	$\sigma_t = 0,\ \sigma_n = 0$	at	$x = L_u + L + L_d,\ 0 \leqslant y \leqslant 1,$

where, far downstream, the normal stress is equal to the pressure, chosen to be zero here. The velocity is prescribed on all boundaries except at the outlet, which is taken to be stress free (σ_t is tangential stress), and on the elastic section, where x_w and y_w are the membrane coordinates of a general point on the wall, which are updated during the computation using the method of spines (Luo & Pedley 1996).

Strictly speaking, the direction of the velocity on the elastic section is not known in our model since a membrane equation is used to describe the wall mechanics and individual elements of the membrane are not tracked. For simplicity, therefore, we make a further *ad hoc* assumption: we assume that the wall points always move in the direction normal to its surface. This is approximately consistent with the constant-tension assumption used here and is in fact exact if the wall shape remains circular. Results obtained with this assumption differed very little from those obtained on the assumption that wall points move only in the y-direction (Luo & Pedley 1996).

For values of Re much greater than 1, as in most cases examined here, the stress-free condition at the downstream end is the best choice for simulating the corresponding experiments where the downstream pressure is fixed, though care must be taken to make L_d sufficiently large (see Luo & Pedley 1996).

For every time-dependent computation, the initial condition was taken to be the computed steady state for a slightly different value of T (tension). As T is decreased, therefore, one can determine critical conditions for instability by finding the first value of T for which the perturbation does not decay to zero.

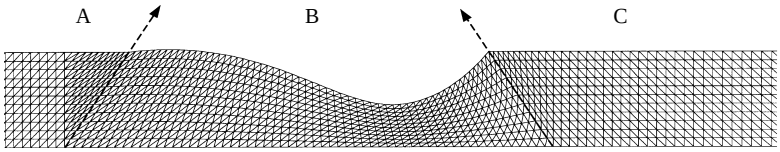

FIGURE 2. Part of a typical adaptive mesh of the flow domain. There are 5060 triangular elements and 10603 nodes, with 2829 movable nodes located in section B.

2.4. *Parameters*

The parameters used here are the same as in the previous unsteady flow study (Luo & Pedley 1996). However, to concentrate on the effects of wall inertia, here we will only consider cases with $Re = 300$. Hence the corresponding dimensionless parameters are

$$L_u = 5, \quad L = 5, \quad L_d = 30, \quad Re = 300, \quad T = 178.916/\beta, \quad p_e - p_d = 1.953,$$

where β is a parameter ($\geqslant 1$) which is increased in order to investigate the effect of lowering membrane tension. The numerical constants in T and $p_e - p_d$ arose from the desire to compare the results of Luo & Pedley (1995, 1996) with those of Lowe & Pedley (1995), who used a different non-dimensionlization. In the previous study, it was found that for a tension with $\beta > \beta_c$, where β_c is a critical value ($\beta_c = 27.5$ for $Re = 300$), steady flow gives way to self-excited oscillations (Luo & Pedley 1996). Three values of β were investigated in detail for a massless membrane: these were $\beta = 30$, 32.5 and 35, named as Case I, Case II, and Case III, respectively. Here we will investigate these cases again with wall inertia, plus cases at a higher value of tension ($\beta = 25$).

3. Methods

The method of solving the unsteady problem when the wall has no mass has been described in detail in a previous paper (Luo & Pedley 1996) where a simultaneous approach is employed, i.e. the fluid and wall motions are computed together. The movable mesh is made adaptive by using the method of spines in a mixed Lagrangian–Eulerian reference frame (Rast 1994; Silliman 1979; Ruschak 1980; Saito & Scriven 1981). A second-order predictor-corrector difference scheme with a variable time increment controlled by the error tolerance is used to solve the time-dependent coupling problem (Gresho, Lee & Sani 1979). In this section, we will concentrate on how to incorporate the inertia term of the membrane into the numerical scheme.

The flow domain is divided into three six-node triangular finite element subdomains (figure 2). Subdomains A and C have nodes fixed in space, while subdomain B, under the elastic section, contains the mesh with moving nodes.

The elemental nodes under the elastic section lie along the spines which emanate from a fixed origin O_s. Each spine k is defined by the Cartesian coordinates of its base point, x_b^k and $y_b^k (= 0)$, and the direction from that point to the origin. The position of node i on spine k is given in terms of a fixed fraction ω_i^k of the spine height h^k as

$$x_i^k = x_b^k + \alpha_x^k \omega_i^k h^k, \tag{6}$$

$$y_i^k = y_b^k + \alpha_y^k \omega_i^k h^k, \tag{7}$$

where $\boldsymbol{\alpha} = (\alpha_x^k, \alpha_y^k)$ is the direction vector of spine k, and the spine height is simply the distance from the spine base to the elastic surface in the direction of $\boldsymbol{\alpha}$. Each spine height is an unknown in the problem and is to be determined as part of the solution.

The variables are as usual expanded isoparametrically in area coordinates, (ζ, η), employing a mixed interpolation, with u, v, x, and y sharing quadratic and p linear expansions,

$$u = \sum_{i=1}^{6} u_i N_i(\zeta, \eta), \quad v = \sum_{i=1}^{6} v_i N_i(\zeta, \eta), \quad p = \sum_{i=1}^{3} p_i L_i(\zeta, \eta), \tag{8}$$

$$x = \sum_{i=1}^{6} x_i(h, \theta) N_i(\zeta, \eta), \quad y = \sum_{i=1}^{6} y_i(h, \theta) N_i(\zeta, \eta), \tag{9}$$

where L_i and N_i are linear and quadratic shape functions respectively, and θ is the angle of a spine with the vertical (Rast 1994). Boundary elements are oriented so that three nodes ($l = 3$, 5 and 2) lie along the elastic membrane. The coordinates of all nodes below the elastic boundary depend on the boundary position, therefore ϕ, $\hat{\boldsymbol{n}}$, ds, and the Jacobian of the coordinate transformation for those elements which contain these nodes, are all functions of x and y, hence of the spine height h.

As the Newton–Raphson method is used to solve the finite element equations of the whole system simultaneously, we need to find the inertia term $m\partial^2\eta/\partial t^2$ in (3) explicitly in terms of $\mathrm{d}h/\mathrm{d}t$, so that we can evaluate the Jacobian matrix analytically rather than having to extrapolate the wall movement during each time step, which would introduce additional errors.

Assuming that the wall points move in the normal direction, we have

$$\frac{\partial \eta}{\partial t} = u_n = u n_x + v n_y \tag{10}$$

in which u_n is the normal velocity of the membrane, u and v are the x- and y-components of fluid velocity on the wall at the point in question, and n_x and n_y are the components of the normal vector. Here the normal is a function of time and spine height h, and the second derivative of the displacement becomes

$$\frac{\partial^2 \eta}{\partial t^2} = \frac{\partial u}{\partial t} n_x + \frac{\partial v}{\partial t} n_y + \frac{\partial n_x}{\partial t} u + \frac{\partial n_y}{\partial t} v. \tag{11}$$

As the mesh is moving with time, the time derivatives of the velocity need to be transformed further into the mixed Eulerian–Lagrangian reference frame (Luo & Pedley 1996)

$$\frac{\partial u}{\partial t} = \frac{\delta u}{\delta t} - \left(\alpha_x^k \frac{\partial u}{\partial x} + \alpha_y^k \frac{\partial u}{\partial y} \right) \frac{\mathrm{d}h^k}{\mathrm{d}t},$$

$$\frac{\partial v}{\partial t} = \frac{\delta v}{\delta t} - \left(\alpha_x^k \frac{\partial v}{\partial x} + \alpha_y^k \frac{\partial v}{\partial y} \right) \frac{\mathrm{d}h^k}{\mathrm{d}t},$$

where $\delta/\delta t$ denotes a rate of change along the spines, while $\partial/\partial t$ is defined in the Eulerian reference frame. Notice that the second part of these expressions represents the movement of the nodes in the moving domain. The derivatives of the normal vector are

$$\frac{\partial n_x}{\partial t} = \frac{\partial \left(\dfrac{\partial y}{\partial L_3} \Big/ \dfrac{\partial s}{\partial L_3} \right)}{\partial t} = \frac{\dfrac{\partial}{\partial t}\left(\dfrac{\partial y}{\partial L_3}\right)\left(\dfrac{\partial x}{\partial L_3}\right)^2 - \dfrac{\partial}{\partial t}\left(\dfrac{\partial x}{\partial L_3}\right)\dfrac{\partial x}{\partial L_3}\dfrac{\partial y}{\partial L_3}}{\left(\dfrac{\partial s}{\partial L_3}\right)^3}, \tag{12}$$

$$\frac{\partial n_y}{\partial t} = \frac{\partial\left(-\dfrac{\partial x}{\partial L_3}\Big/\dfrac{\partial s}{\partial L_3}\right)}{\partial t} = \frac{\dfrac{\partial}{\partial t}\left(\dfrac{\partial y}{\partial L_3}\right)\left(\dfrac{\partial x}{\partial L_3}\right)\left(\dfrac{\partial y}{\partial L_3}\right) - \dfrac{\partial}{\partial t}\left(\dfrac{\partial x}{\partial L_3}\right)\left(\dfrac{\partial y}{\partial L_3}\right)^2}{\left(\dfrac{\partial s}{\partial L_3}\right)^3}, \quad (13)$$

where L_3 is the shape function along the elastic boundary, $(\partial s/\partial L_3)^2 = (\partial x/\partial L_3)^2 + (\partial y/\partial L_3)^2$ and $\partial/\partial t(\partial x/\partial L_3)$, $\partial/\partial t(\partial y/\partial L_3)$ can be expressed in terms of $\mathrm{d}h/\mathrm{d}t$ through equations (7), (9) and (11):

$$\frac{\partial}{\partial t}\left(\frac{\partial x}{\partial L_3}\right) = \sum_{i=1}^{6}\sum_{k=1}^{3}\alpha_x^k\frac{\partial N_i}{\partial L_3}\frac{\mathrm{d}h^k}{\mathrm{d}t}\quad \frac{\partial}{\partial t}\left(\frac{\partial y}{\partial L_3}\right) = \sum_{i=1}^{6}\sum_{k=1}^{3}\alpha_y^k\frac{\partial N_i}{\partial L_3}\frac{\mathrm{d}h^k}{\mathrm{d}t}. \quad (14)$$

Therefore in the formulation of the finite element matrix, the residual vector

$$\boldsymbol{R} = (R_x, R_y, R_c, R_e)^T,$$

obtained using the Galerkin residual method, where the subscripts x, y, c, and e indicate the corresponding residual of the x- and y-momentum, continuity, and membrane equation, respectively, is the same as described by Luo & Pedley (1996) except that the membrane residual term R_e at the element level now becomes

$$\begin{aligned}
R_e^l = &\int mN_l\left(\frac{\partial u}{\partial t}n_x + \frac{\partial v}{\partial t}n_y + \frac{\partial n_x}{\partial t}u + \frac{\partial n_y}{\partial t}v\right)\mathrm{d}s \\
&+P_e\int N_l\mathrm{d}s - \sum_{j=2}^{3}\sigma_{nj}\int N_lL_j\mathrm{d}s - T\sum_{j=1}^{3}\int N_lL_j\frac{\partial\phi}{\partial s}\mathrm{d}s \\
= &\sum_{i=1}^{6}\frac{\delta u_i}{\delta t}m\int N_lN_in_x\mathrm{d}s - \sum_{i=1}^{6}\sum_{k=1}^{3}u_i\frac{\mathrm{d}h_k}{\mathrm{d}t}m\int N_ln_x\left(\alpha_x\frac{\partial N_i}{\partial x} + \alpha_y\frac{\partial N_i}{\partial y}\right)\mathrm{d}s \\
&+\sum_{i=1}^{6}\frac{\delta v_i}{\delta t}m\int N_lN_in_y\mathrm{d}s - \sum_{i=1}^{6}\sum_{k=1}^{3}v_i\frac{\mathrm{d}h_k}{\mathrm{d}t}m\int N_ln_y\left(\alpha_x\frac{\partial N_i}{\partial x} + \alpha_y\frac{\partial N_i}{\partial y}\right)\mathrm{d}s \\
&+\sum_{i=1}^{6}\sum_{j=1}^{6}\sum_{k=1}^{3}u_i\frac{\mathrm{d}h^k}{\mathrm{d}t}m\int N_lN_i(n_xn_y\alpha_x^k + n_y^2\alpha_y^k)\frac{\partial N_j}{\partial L_3}\mathrm{d}L_3 \\
&-\sum_{i=1}^{6}\sum_{j=1}^{6}\sum_{k=1}^{3}v_i\frac{\mathrm{d}h^k}{\mathrm{d}t}m\int N_lN_i\left(n_x^2\alpha_x^k + n_xn_y\alpha_y^k\right)\frac{\partial N_j}{\partial L_3}\mathrm{d}L_3 \\
&+P_e\int N_l\mathrm{d}s - \sum_{j=2}^{3}\sigma_{nj}\int N_lL_j\mathrm{d}s - T\sum_{j=1}^{3}\int N_lL_j\frac{\partial\phi}{\partial s}\mathrm{d}s,
\end{aligned}$$

where l denotes the nodal number of the 6-node triangle element used here.

The global finite element matrix equation

$$\boldsymbol{M}\frac{\mathrm{d}\boldsymbol{U}}{\mathrm{d}t} + \boldsymbol{K}(\boldsymbol{U})\boldsymbol{U} - \boldsymbol{F} = \boldsymbol{R}, \quad (15)$$

where $\boldsymbol{U} = \{u, v, p, h\}$, assembled using the frontal technique, is solved with a second-order predictor-corrector time integration scheme with variable time increment and Newton–Raphson iteration. A small value of ϵ ($\leqslant 10^{-5}$–10^{-7}) is chosen as both the convergence criterion for the Newton–Raphson iterations and the tolerance for the time-truncation error (Luo & Pedley 1996).

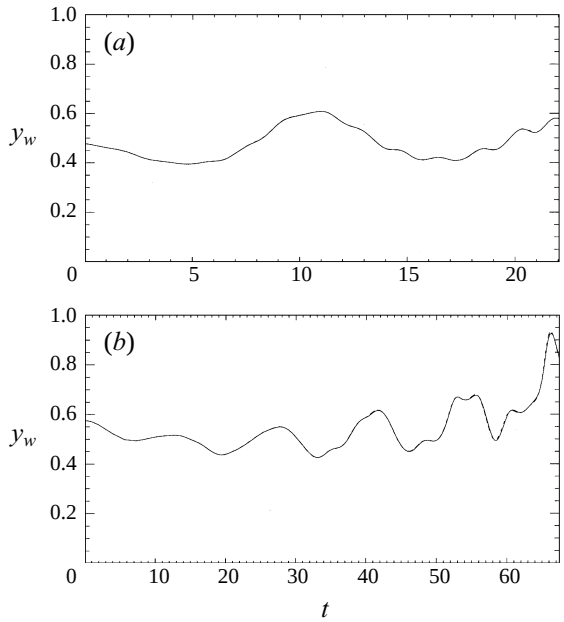

FIGURE 3. Wall position y_w at $x_w = 8.5$ is plotted as a function of time for the two different meshes and for the parameters (*a*) $\beta = 30$, $m = 0.1$, and (*b*) $\beta = 25$, $m = 1.0$. Results from the two different meshes are graphically almost indistinguishable.

3.1. *Computational accuracy*

The accuracy of the numerical code used here has been tested extensively over both space and time for the time-dependent simulation with massless membrane (Luo & Pedley 1996). Here however, we have re-tested the code to make sure that the grid size and time increments are suitable for the coupled membrane–fluid motion when wall inertia is included. This is because wall inertia is found to cause some small-amplitude, high-frequency flutter, which may need higher resolution.

The typical grid used has 5060 six-node triangular elements and 10 603 nodes, with 2829 movable nodes (682 elements) located in section B, shown in figure 2. This is the grid that was tested for many cases and was considered satisfactory for the parameters of interest when wall inertia is absent. A quick way of checking whether this grid is good enough when wall inertia is included is to use a different grid with fewer elements and compare the results. The grid we used for comparison has 4576 elements and 9591 nodes, with 1909 movable nodes (462 elements) located in section B. Note that the upstream section A and downstream section C remain unchanged in the two grids, while in section B the number of nodes has been reduced to be about 67% in the grid for comparison. The results obtained from the two grids are plotted in figure 3(*a*, *b*) for two different cases. It is clear that the results are independent of grid size.

To check the temporal accuracy of the solution, we have checked for different values of ϵ in the range of 10^{-5}–10^{-8}, for $Re = 300$, $\beta = 25$, and $m = 0.1$. This is the case when high frequency flutter is induced, purely due to the introduction of wall inertia (see below). The wall oscillations obtained for $\epsilon = 10^{-5}$, 10^{-6}, 10^{-7} and 10^{-8} are shown in figure 4. Because the fluid motion downstream (vorticity waves) is very sensitive to small numerical perturbations (Tutty & Pedley 1993), it is not

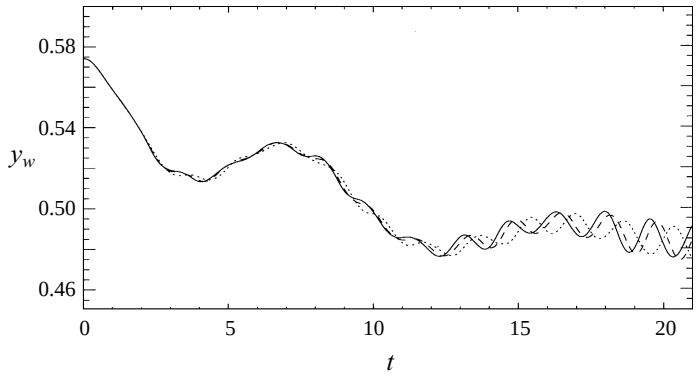

FIGURE 4. Wall position y_w at $x_w = 8.5$ is plotted as a function of time with error tolerance $\epsilon = 10^{-5}$ (dotted), $\epsilon = 10^{-6}$(dashed) $\epsilon = 10^{-7}$ (dash-dotted) and $\epsilon = 10^{-8}$ (solid) for $\beta = 25$, and $m = 0.1$. Results from $\epsilon = 10^{-7}$ and $\epsilon = 10^{-8}$ are graphically indistinguishable.

surprising here to observe the ϵ dependence. We found, as they did, that to obtain a fully converged solution which does not depend on the value of ϵ, ϵ has to be set extremely small. Figure 4 shows that for $m = 0.1$, only when $\epsilon < 10^{-7}$ do the results start to look graphically indistinguishable for the period of time plotted. However, it is noted that, between $\epsilon = 10^{-5}$ and $\epsilon = 10^{-7}$, there are only small phase differences in the presented results, indicating that different levels of numerical error can trigger the instabilities at different times, but without affecting the disturbance amplitude. Keeping in mind that our main aim at this stage is still to try to understand the qualitative behaviour, rather than to produce detailed results for the system, we have minimized the computing cost in the following results by using $\epsilon = 10^{-7}$ only for cases with $m = 0.1$; $\epsilon = 10^{-5}$ is used for all other cases, in which relatively gentle oscillations are expected.

4. Results

4.1. $m = 0.01$

We look first at the case when m is small, say, $m = 0.01$. This may be relevant to experiments conducted with water flowing through a rubber tube, because the volume densities of water and rubber are of the same order and, if the ratio of membrane thickness w to channel height D is taken to be 10^{-2}, then $m = \rho_w w/\rho D$ should be 10^{-2} also, though note the above proviso that quantitative agreement with tube flow experiments is unlikely. The aim here is to see if including the wall inertia would have any significant influence on the self-excited oscillations found previously (Luo & Pedley 1996).

Figure 5 shows the wall position y_w close to the site of maximum deformation, $x_w = 8.5$, as a function of time t, when $\beta = 30$. The solid curve gives the result with $m = 0.01$, and the dashed curve is the one with $m = 0$, i.e. without wall inertia. It is clear that there is no significant change for this value of m. A similar finding is obtained for other values of β. In other words, it is probably reasonable to ignore the wall inertia when modelling blood flow in collapsible vessels and the related laboratory experiments.

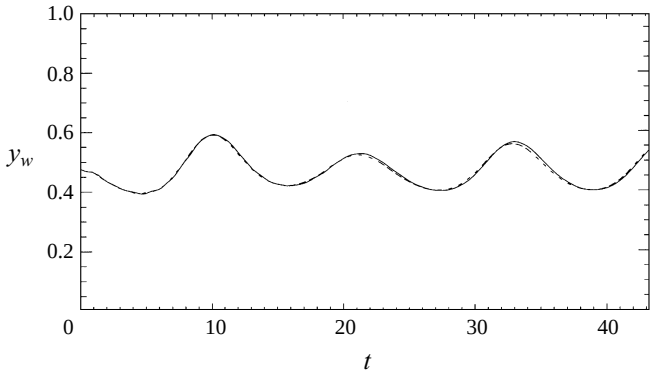

FIGURE 5. Wall position y_w at $x_w = 8.5$ is plotted as a function of time obtained for small density ratio $m = 0.01$ at $\beta = 30$, compared with the same results with $m = 0$ (broken line).

4.2. $m = 0.1$

Cases I–III: Flutter at a lower tension $\beta > \beta_c$

This case is more relevant to flow through a thin rubber tube of a less dense fluid, though probably not when density is as low as that of air. In order to compare with the three cases investigated earlier (Luo & Pedley 1996), here we present the typical results for Case I: $\beta = 30$, Case II: $\beta = 32.5$, and Case III: $\beta = 35$, respectively. All the solid lines in the figures represent the results obtained with $m = 0.1$, and the dashed lines are those with zero m.

Figures 6 and 7 show the results obtained for Case I. The wall position y_w at $x_w = 8.5$ is plotted as a function of time t in figure 6(a), and the evolution of the whole elastic wall shape with time during one of the periods, marked as a darker line from t_1 to t_2 in figure 6(a), is plotted in figure 6(b). The corresponding wall pressure at $x_w = 8.5$ is also plotted as a function of time in figure 7(a), and the evolution of the pressure drop along the elastic wall is shown in figure 7(b). Figure 8 and figure 9 give the corresponding results for Cases II and III, respectively. However, in figures 8 and 9 only the point evolution of the wall motion and pressure (as in figures 6a and 7a) is presented.

From figures 6–9, we can see that there appears to be some higher-frequency and smaller-amplitude oscillation, or flutter, which initially is superimposed on the original large-amplitude slower mode, i.e. tension-induced oscillations, and then becomes larger, eventually dominating the original mode. Most of these oscillations are not periodic. However, by assuming periodicity of the wave from t_1 to t_2, see figures 6 and 7, we can perform a fast Fourier transform of the data and find the important dimensionless frequencies present. The frequency of the flutter in Case I is about 0.55, six times higher than the fundamental frequency of the slower oscillation, which is about 0.084. There seem to be two higher frequencies for the flutter in Case II, namely 0.51 and 0.71, which are five and seven times the fundamental frequency of the slower oscillation, respectively. The duration of the computation in Case III (figure 9) was not long enough for a fast Fourier transform to be useful, though there is evidence of some flutter.

The oscillations of the wall coordinate y_w and wall pressure p_w are slightly out of phase in the flutter modes, but are roughly in phase in the slower modes. For the slower modes, this has been explained earlier (Luo & Pedley 1996); for the flutter, the phase difference implies that energy has been irreversibly transferred to the wall.

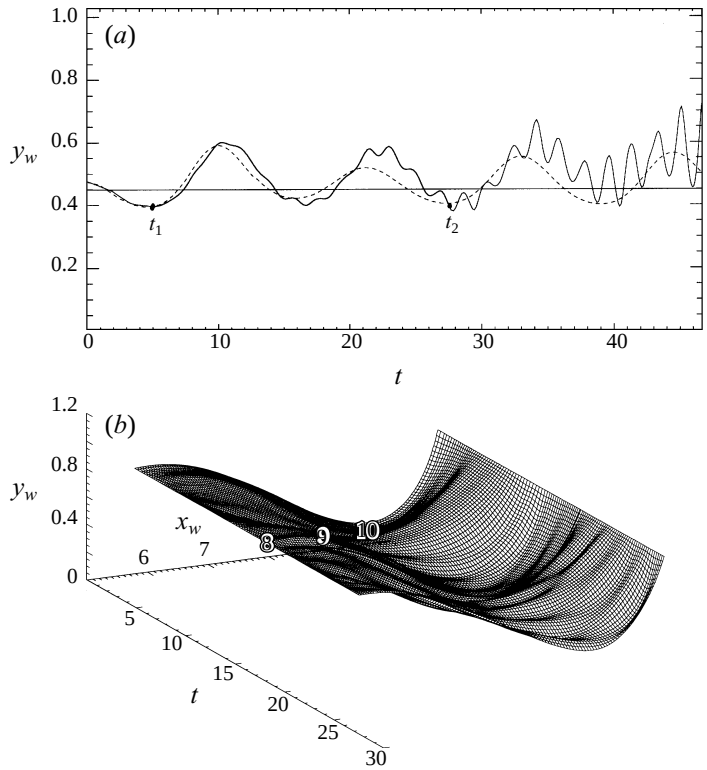

FIGURE 6. Case I: (*a*) wall position at $x_w = 8.5$ plotted as a function of time for $m = 0.1$, $\beta = 30$ (solid), compared with the corresponding result for $m = 0$ (broken), and the steady solution (horizontal line); (*b*) time evolution of the displacement distribution along the elastic wall, during $t = 4.80$–27.34, marked as darker line from t_1 to t_2 in (*a*).

Such irreversible energy transfer occurs during the instability leading to travelling wave flutter in long elastic channels and will be discussed further below.

Compared with the wall motion, the pressure wave seems to be more sensitive to the effects of wall inertia. In all the three cases investigated, flutter appears first in the pressure wave, and then after some time in the wall motion. For Case I, flutter is seen in the pressure wave after $t = 4.8$, and in the wall motion after $t = 7.5$; a similar sequence of events is observed for Case II. For Case III, flutter is only obvious in the pressure wave, not in the wall motion. This is presumably because the computing time was not long enough for flutter to develop in the wall motion. This is interesting, as it suggests that flutter, unlike the oscillations seen in the previous paper (Luo & Pedley 1996), is not a consequence of the generation of vorticity waves downstream (see Pedley & Stephanoff 1985). Here, some waves appear downstream well before flutter is clearly seen in the wall motion: see figures 10–12 for streamline contours in all three cases. Presumably these waves are triggered by the pressure fluctuations at the membrane.

Case IV: Flutter at a higher tension $\beta < \beta_c$

The flutter-type oscillations are observed to be superimposed on the original oscillations for the three cases presented above. In these cases the steady flow was initially (i.e. without wall inertia) unstable at low enough tension. It is interesting also

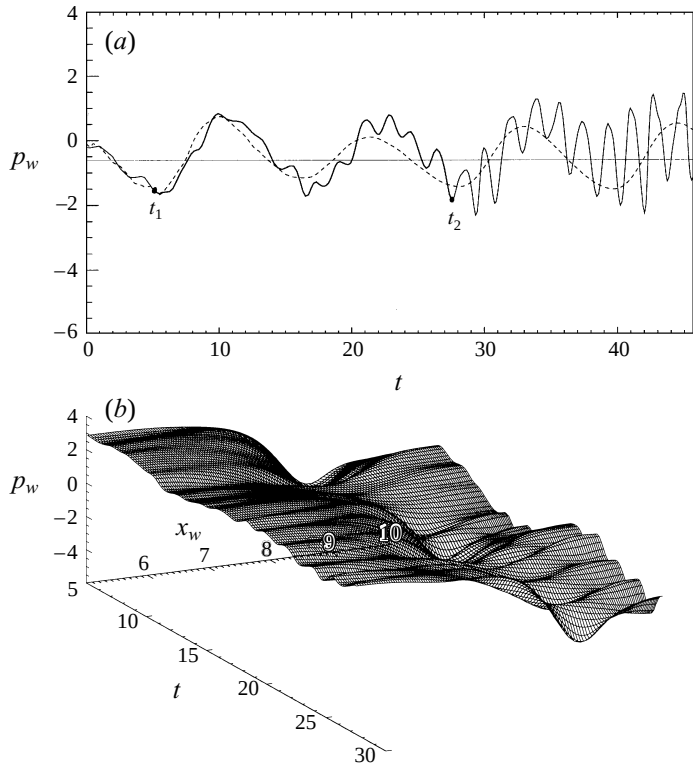

FIGURE 7. Case I: (*a*) wall pressure at $x_w = 8.5$ plotted as a function of time for $m = 0.1$, $\beta = 30$ (solid), compared with the corresponding result for $m = 0$ (broken), and the steady solution (horizontal line); (*b*) time evolution of the pressure distribution along the elastic wall, during $t = 4.80$–27.34, marked as darker line from t_1 to t_2 in (*a*).

to include wall inertia in a flow which was previously stable. We therefore calculated a case, Case IV, with $\beta = 25$, and $m = 0.1$. The wall deformation is shown in figure 13(*a*), and the pressure distribution is shown in figure 13(*b*). Obviously, this is a case when the flow becomes unstable solely due to the presence of the wall inertia, because the corresponding result for $m = 0$, shown as a dotted line in figure 13, is stable and approaches the steady state. There are growing waves both in wall deformation and in the pressure. The exponential growth rate for both is about the same: 0.005.

It is interesting to note that, although the wave in the wall appears to be regular and sinusoidal, with fundamental frequency of about 0.6, it is not quite so regular in the pressure oscillation: see figure 13(*b*). In fact, it looks as if the pressure wave has experienced a kind of period-doubling bifurcation, with one regular wave of frequency of about 0.61, which is slightly out of phase with the wave in the wall, combined with an additional wave of about half the frequency. There are also times when the wavenumbers of wall and wall pressure are different. Figure 14(*a*, *b*) shows the membrane displacement perturbation relative to the initial steady case, $y_w - y_w^0$, and the pressure perturbation along the membrane, $p_w - p_w^0$, at four different times during the flutter. The superscript 0 denotes the initial steady state. The wall wave has a wavenumber $k = 0.4\pi$ at the earlier stage, $t \leqslant 21.41$, i.e. one whole wave for a length of 5 units along the membrane. Then a higher-order wave with wavenumber 0.8π also sets in as the wave grows (after $t = 23.70$). However, in the pressure wave,

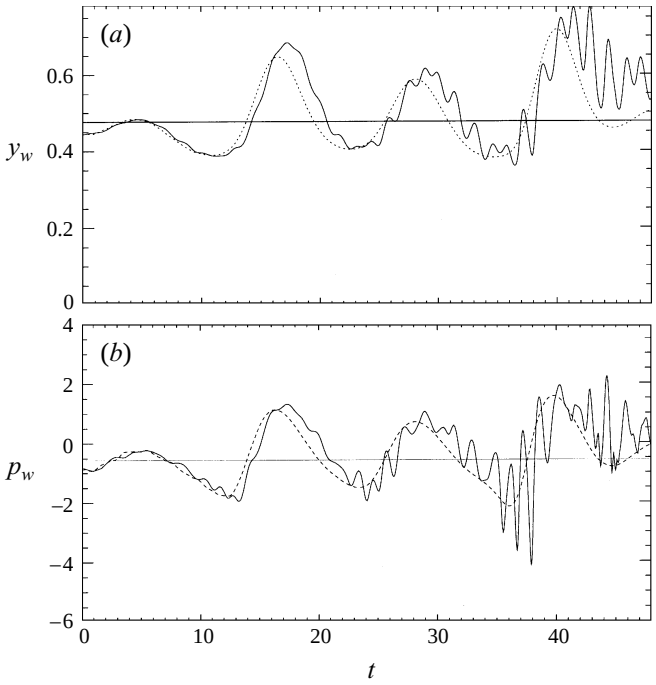

FIGURE 8. Case II: (*a*) wall position y_w, and (*b*) wall pressure, at $x_w = 8.5$, plotted as a function of time for $m = 0.1$, $\beta = 32.5$ (solid), compared with the corresponding result for $m = 0$ (broken), and the steady solution (horizontal line).

the wavenumber k is almost 0.8π at the beginning of the flutter, $t = 21.41$, and then higher-order waves with wavenumbers up to 1.2π are also involved as the flutter grows.

Apparently, the wall inertia at this density ratio, $m = 0.1$, has prominent effects on the nature of the self-excited oscillations. It causes instabilities for significantly higher values of tension. For $Re = 300$, we have ascertained that flutter can appear for β as low as 10, to be compared with a value of 27.5 for a massless wall. Even for much lower tension, where the slow mode oscillations are generated first, the original slow mode soon appears to be dominated by the higher-frequency flutter, so it is the latter that would presumably be observed in experiments. This is consistent with observations on air flow in a rubber tube (Sakurai & Ohba 1986; Ohba *et al.* 1984), though as explained above a direct comparison cannot be made.

4.3. $m = 1$

Case V: Flutter at $m = 1$ with $\beta < \beta_c$

What happens at a larger value of m, say, $m = 1$? Such a value implies that the membrane is thick or much denser than the fluid. Again, we look at the case $\beta = 25$, Case V, which is a stable case for a massless membrane.

The wall displacement is shown in figure 15(*a*). It seems that for this case, the system experiences a rather different and much slower oscillation compared with the cases with $m = 0.1$. The fundamental frequency of the wall oscillation is found to be about 0.077, with a wavenumber about 0.6π during most of the time period in figure 15(*a*), except for the last 10 units of time. The wave grows fast and nonlinearly, with an exponential growth rate which varies between 0.016 and 0.042, and the amplitude

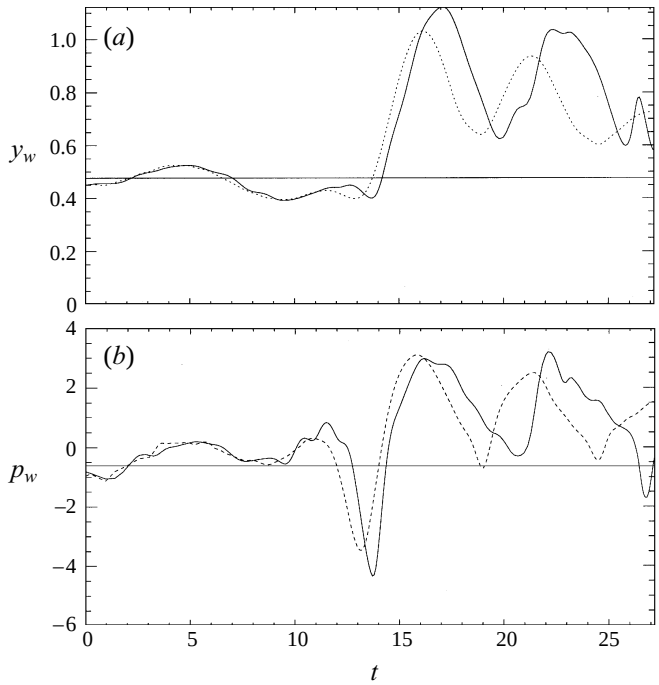

FIGURE 9. Case III: (*a*) wall position y_w, and (*b*) wall pressure, at $x_w = 8.5$, plotted as a function of time for $m = 0.1$, $\beta = 35$, (solid), compared with the corresponding result for $m = 0$ (broken), and the steady solution (horizontal line).

of the oscillation soon becomes too large for the mesh generator to manage. Hence the numerical scheme breaks down due to a rapid variation near the downstream end of the membrane. The frequency of this oscillation is much smaller than for the flutter found above, and is almost comparable to that of the slower modes that arise without wall inertia, although it grows much faster. This implies that, as m increases, the mechanisms of the oscillations may have changed. The fact that increasing the mass ratio actually reduces the flutter frequency has also been observed by Grotberg and co-workers, who applied a linear theory to flow in a two-dimensional flexible channel, and found that a larger wall mass is destabilizing, but heavier walls tend to diminish the flutter frequency towards zero (Grotberg & Reiss 1984).

It should be repeated that the present model is somewhat artificial, and has only tenuous physiological application. In particular, as the wall thickness increases, the membrane model itself becomes questionable, even in two dimensions, as the bending stiffness and wall damping are no longer negligible. Nevertheless, it serves to demonstrate some possible transitions of oscillation type as the density ratio increases.

5. Discussion

Comparison with linear theories.

It is reasonable to suppose that, if the wall mass parameter, m, were very large, the membrane would oscillate like a stretched string, virtually unaffected by the fluid loading. As m is reduced the fluid loading will become more significant, both modifying the oscillations and generating new ones.

Instabilities of flow past compliant boundaries have been analysed by many authors

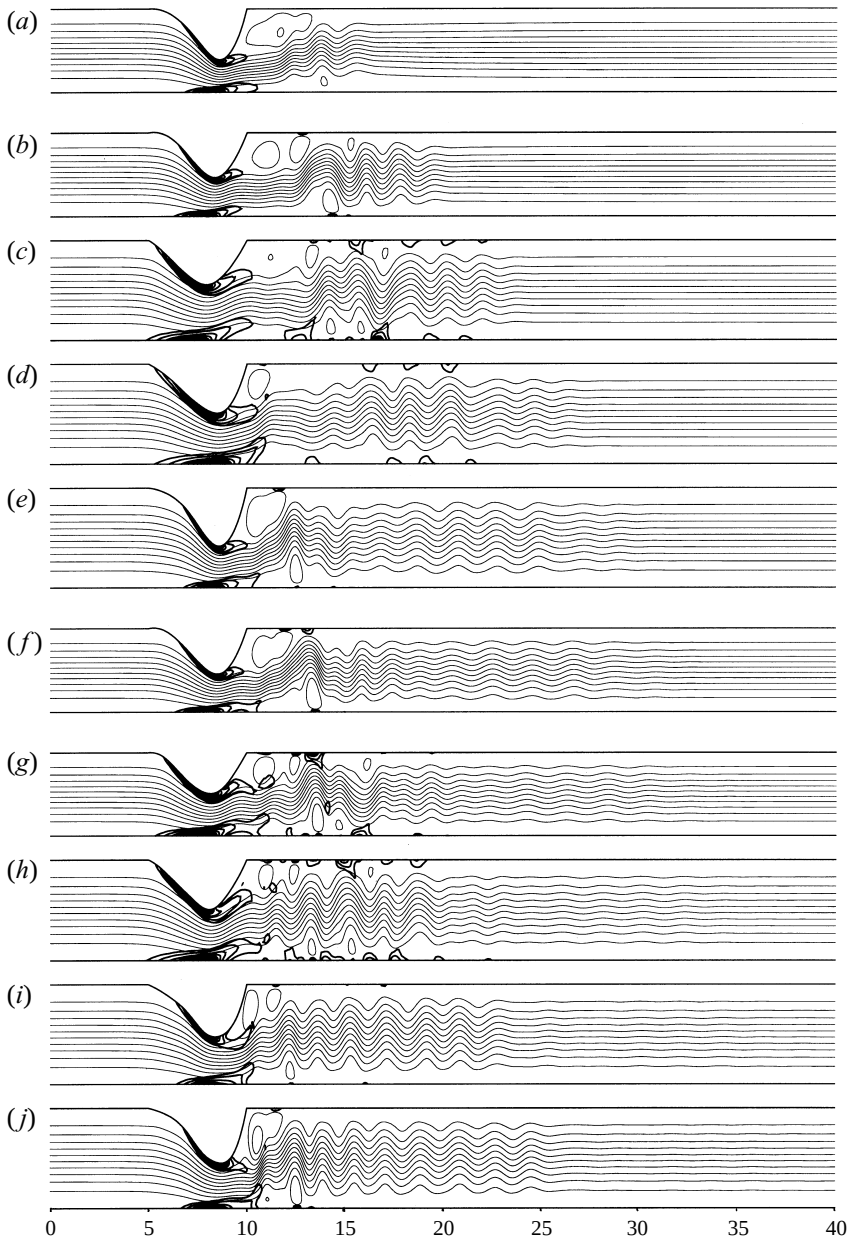

FIGURE 10. Instantaneous streamlines (lighter lines) and energy dissipation contours (darker lines) for Case I. Fifteen equally spaced streamlines are plotted between ψ_{max} and ψ_{min}, and fourteen energy dissipation contours are plotted between 0 and Φ_{max}, during the period $t = 4.80$–27.34:

(a) $t = 4.80$, $\psi_{max} = 1.12$, $\psi_{min} = -0.022$, $\Phi_{max} = 16.65$;
(b) $t = 7.58$, $\psi_{max} = 1.08$, $\psi_{min} = -0.073$, $\Phi_{max} = 12.44$;
(c) $t = 11.32$, $\psi_{max} = 1.05$, $\psi_{min} = -0.03$, $\Phi_{max} = 4.40$;
(d) $t = 13.16$, $\psi_{max} = 1.06$, $\psi_{min} = -0.01$, $\Phi_{max} = 4.23$;
(e) $t = 16.32$, $\psi_{max} = 1.09$, $\psi_{min} = -0.07$, $\Phi_{max} = 14.36$;
(f) $t = 18.56$, $\psi_{max} = 1.09$, $\psi_{min} = -0.11$, $\Phi_{max} = 12.72$;
(g) $t = 20.70$, $\psi_{max} = 1.08$, $\psi_{min} = -0.09$, $\Phi_{max} = 4.83$;
(h) $t = 22.81$, $\psi_{max} = 1.06$, $\psi_{min} = -0.03$, $\Phi_{max} = 4.02$;
(i) $t = 25.19$, $\psi_{max} = 1.08$, $\psi_{min} = -0.04$, $\Phi_{max} = 9.04$;
(j) $t = 27.34$, $\psi_{max} = 1.18$, $\psi_{min} = -0.08$, $\Phi_{max} = 12.01$.

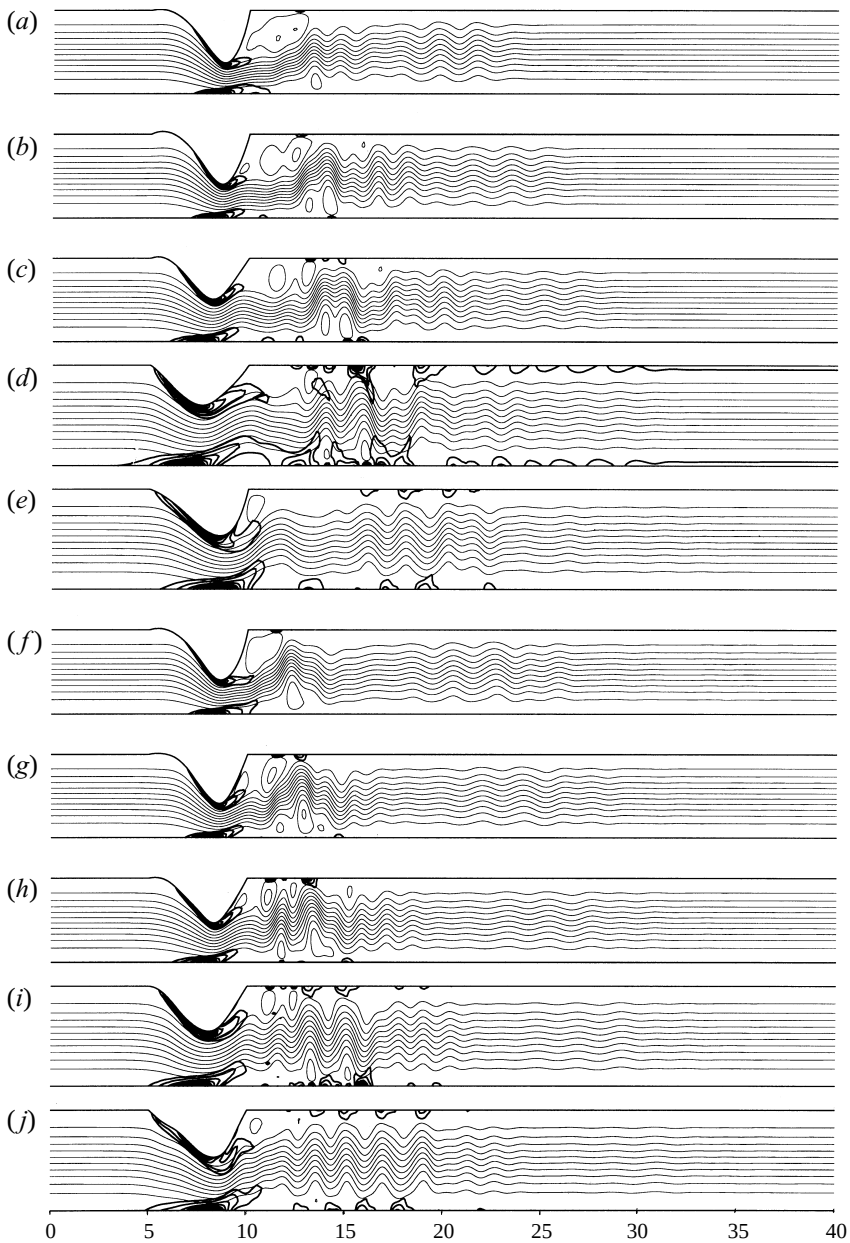

FIGURE 11. As figure 10 but Case II, during the period $t = 10.81$–30.8:
(*a*) $t = 10.81$, $\psi_{max} = 1.11$, $\psi_{min} = -0.04$, $\Phi_{max} = 19.83$;
(*b*) $t = 13.00$, $\psi_{max} = 1.13$, $\psi_{min} = -0.10$, $\Phi_{max} = 20.18$;
(*c*) $t = 15.03$, $\psi_{max} = 1.08$, $\psi_{min} = -0.08$, $\Phi_{max} = 9.17$;
(*d*) $t = 17.19$, $\psi_{max} = 1.05$, $\psi_{min} = -0.04$, $\Phi_{max} = 2.48$;
(*e*) $t = 19.93$, $\psi_{max} = 1.04$, $\psi_{min} = -0.01$, $\Phi_{max} = 3.51$;
(*f*) $t = 22.93$, $\psi_{max} = 1.03$, $\psi_{min} = -0.07$, $\Phi_{max} = 15.77$;
(*g*) $t = 24.85$, $\psi_{max} = 1.13$, $\psi_{min} = -0.19$, $\Phi_{max} = 15.30$;
(*h*) $t = 26.65$, $\psi_{max} = 1.15$, $\psi_{min} = -0.06$, $\Phi_{max} = 11.70$;
(*i*) $t = 28.51$, $\psi_{max} = 1.09$, $\psi_{min} = -0.04$, $\Phi_{max} = 4.37$;
(*j*) $t = 30.80$, $\psi_{max} = 1.02$, $\psi_{min} = -0.01$, $\Phi_{max} = 3.90$.

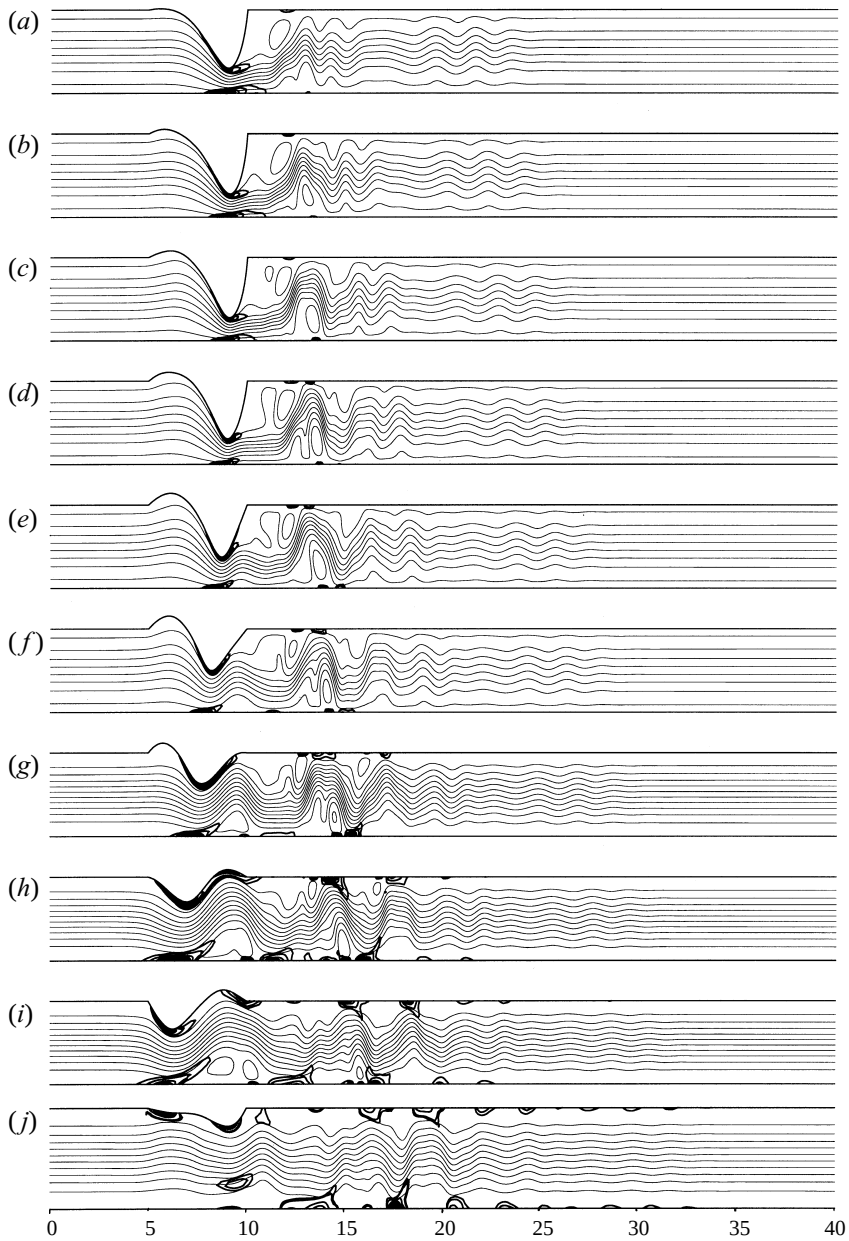

FIGURE 12. As figure 10 but for Case III, during the period $t = 10.41$–18.60:
(*a*) $t = 10.41$, $\psi_{max} = 1.19$, $\psi_{min} = -0.09$, $\Phi_{max} = 34.29$;
(*b*) $t = 11.14$, $\psi_{max} = 1.20$, $\psi_{min} = -0.15$, $\Phi_{max} = 49.81$;
(*c*) $t = 11.97$, $\psi_{max} = 1.19$, $\psi_{min} = -0.22$, $\Phi_{max} = 59.26$;
(*d*) $t = 12.70$, $\psi_{max} = 1.20$, $\psi_{min} = -0.21$, $\Phi_{max} = 65.55$;
(*e*) $t = 13.50$, $\psi_{max} = 1.18$, $\psi_{min} = -0.21$, $\Phi_{max} = 43.53$;
(*f*) $t = 14.31$, $\psi_{max} = 1.13$, $\psi_{min} = -0.17$, $\Phi_{max} = 26.78$;
(*g*) $t = 15.24$, $\psi_{max} = 1.09$, $\psi_{min} = -0.12$, $\Phi_{max} = 10.67$;
(*h*) $t = 16.15$, $\psi_{max} = 1.05$, $\psi_{min} = -0.09$, $\Phi_{max} = 4.90$;
(*i*) $t = 17.26$, $\psi_{max} = 1.01$, $\psi_{min} = -0.05$, $\Phi_{max} = 3.99$;
(*j*) $t = 18.60$, $\psi_{max} = 1.01$, $\psi_{min} = -0.01$, $\Phi_{max} = 1.68$.

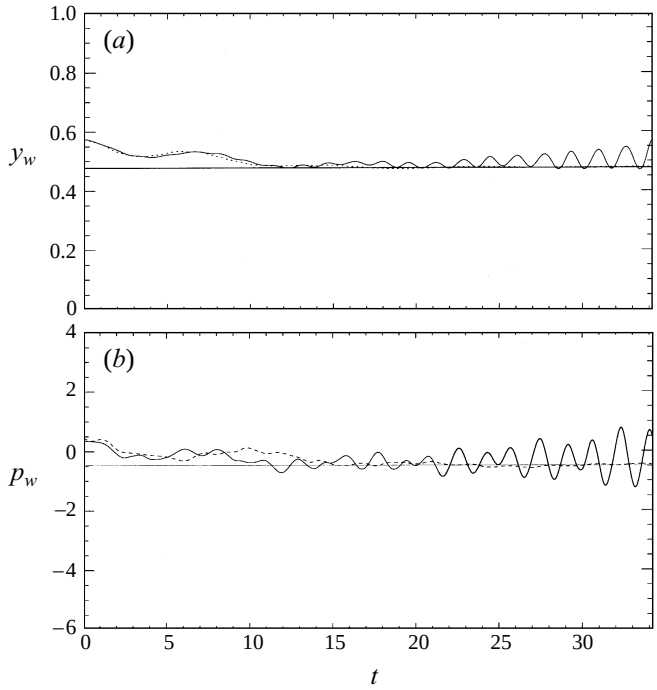

FIGURE 13. Cast IV (*a*) wall position y_w, and (*b*) wall pressure, at $x_w = 8.5$, plotted as a function of time for $m = 0.1$, $\beta = 25$, compared with the corresponding result for $m = 0$ (dotted), and the steady solution (horizontal line).

(Carpenter & Garrad 1986; Carpenter & Morris 1990; Weaver & Paidoussis 1977; Gavriely *et al.* 1989; Grotberg & Reiss 1984; Grotberg & Shee 1985; LaRose & Grotberg 1997; Lucey & Carpenter 1992; Davies 1995; Davies & Carpenter 1997*a*, *b*), though usually for infinitely long compliant boundaries, and invariably with a basic, undisturbed state of parallel flow with a planar boundary, not steady separated flow past a finite, indented membrane as here. Nevertheless, it will be instructive to compare the frequencies of the modes found numerically with those predicted by relevant linear theories.

The (radian) frequencies of a stretched membrane of length L, tension T and mass m per unit length, in the absence of fluid loading, are given by

$$\omega_0^2 = \frac{(n\pi)^2 T}{L^2 m}, \tag{16}$$

where n is an integer (the mode number) and the parameters can be regarded as either dimensional or dimensionless.

An approximate way of accounting for inviscid fluid loading, in the absence of a mean flow, is to consider an infinite elastic channel, of width 1, along which linear waves of wavenumber k can propagate in either direction with frequency ω, where ω is determined by using a theory like that for waves on water of finite depth under surface tension (Acheson 1990):

$$\omega^2 = \frac{Tk^2}{(m + 1/(k \tanh k))}. \tag{17}$$

A similar theory, but with additional wall properties and, notably, a 'Darcy friction'

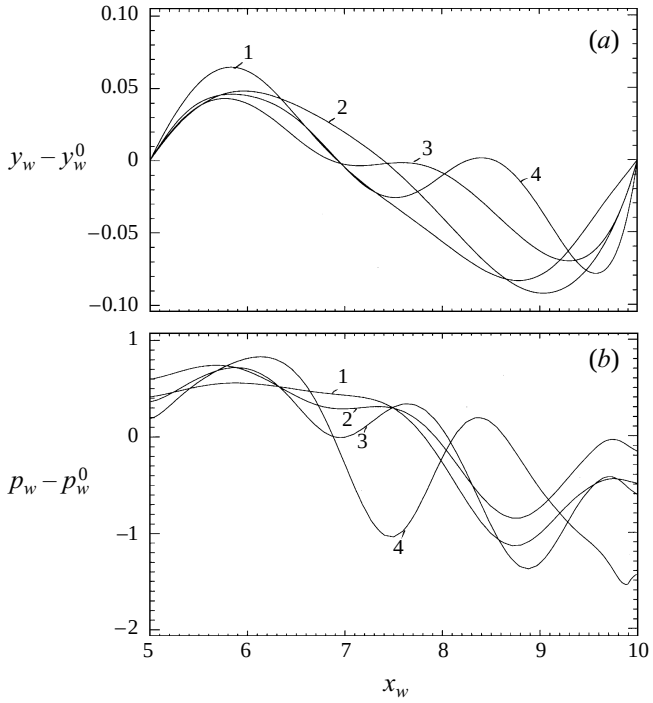

FIGURE 14. Case IV: (*a*) the spatial wave of the wall y_w minus the corresponding steady state y_w^0 at four different times, curve 1: $t = 21.41$, 2: $t = 24.93$, 3: $t = 31.15$, 4: $t = 34.23$, (*b*) the spatial wave of the pressure along the wall p_w minus the corresponding steady state p_w^0 at the same times.

model for fluid viscosity, was derived by Grotberg & Reiss (1984). The case of a finite membrane of length L can be modelled by superposing two waves, of equal amplitudes but opposite propagation directions, in such a way that the membrane displacement is zero at $x = 0$ and $x = L$ (Davies & Carpenter 1997*a*). The frequencies are then given by (17) with

$$k = \frac{n\pi}{L}. \tag{18}$$

Adding a mean flow with uniform speed U replaces ω in (17) by $\omega \pm kU$, so that positive and negative travelling waves with the same frequency have different wavenumbers, say $k_+(\omega)$ and $k_-(\omega)$. The requirement that the displacement is zero at $x = 0$, L then gives

$$k_+ + k_- = \frac{2n\pi}{L}, \tag{19}$$

which constitutes an eigenvalue equation for ω, though it cannot be solved explicitly.

A more accurate model takes account of the parabolic velocity profile in the oncoming flow, so that the dispersion relation for a propagating wave is not (17) with ω replaced by $\omega \pm kU$ but is obtained by solving the Rayleigh equation with membrane boundary conditions. When viscosity is taken into account, moreover, so that the governing equation becomes the Orr–Sommerfeld equation, additional modes come into play (Tollmien–Schlichting waves, modified by the membrane).

In their approximate solution, Davies & Carpenter (1997*b*) (following Green & Ellen 1972) used the first two terms of Heisenberg's (1924) small-k expansion as the solution to the Rayleigh equation, but with compliant wall boundary conditions. In

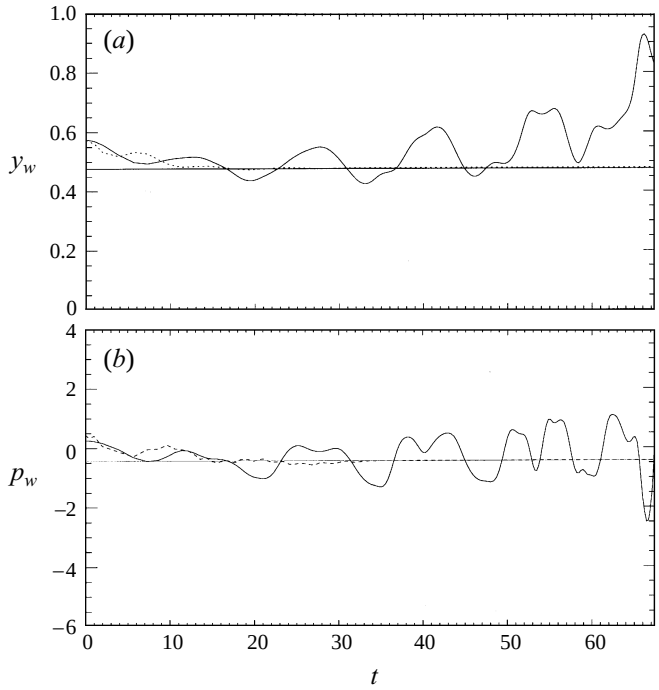

FIGURE 15. Case V: (*a*) wall position y_w, and (*b*) wall pressure, at $x_w = 8.5$, for $\beta = 25$, $m = 1$ (solid), compared with the corresponding result for $m = 0$ (dotted), and the steady solution (horizontal line). The numerical scheme breaks down at $t = 67.44$.

terms of our variables, their result is that downstream and upstream propagating waves of radian frequency ω have wavenumbers k_+ and k_- given by

$$k_\pm = \frac{\omega(1+2m)}{r \pm 1}, \tag{20}$$

where

$$r = \left((1+2m)2T - \frac{1+12m}{5}\right)^{1/2}. \tag{21}$$

For zero displacement at $x = 0$, L, k_+ and k_- must again satisfy (19), from which we obtain the explicit formula

$$\omega = 2\pi n \frac{T - \frac{3}{5}}{Lr}. \tag{22}$$

Table 1 lists the frequencies f $(= \omega/2\pi)$ obtained from each of equations (16), (17), (19) and (22), for comparison with our computed frequencies (top row). It can be seen that, for all four cases with $m = 0.1$ (Cases I–IV), the models which take account of fluid loading all predict frequencies that, for $n = 2$, agree reasonably well with the predictions of the full computations. Moreover the wavenumber k $(= n\pi/L)$ is 0.4π for $n = 2$ and $L = 5$, which also agrees quite well with the numerical result (see figure 14). The best agreement is achieved by the Davies & Carpenter (1997*b*) result (22) (rather surprisingly, equation (17) does better than equation (19), although the latter takes some account of fluid flow). None of the models does well for Case V ($m = 1.0$), however. Presumably the slow, growing oscillations in that case are not modified stretched-string vibrations, but represent a different mode altogether.

Case	I	II	III	IV	V
2D	0.554	0.506, 0.709	0.486	0.6012	0.0512
Equation (16) $n = 1$	0.772	0.742	0.715	0.846	0.267
$n = 2$	1.544	1.454	1.430	1.692	0.535
Equation (17) $n = 1$	0.141	0.135	0.131	0.155	0.136
$n = 2$	0.479	0.461	0.444	0.526	0.385
Equation (19) $n = 1$	0.118	0.113	0.105	0.134	0.100
$n = 2$	0.439	0.419	0.400	0.489	0.309
Equation (22) $n = 1$	0.288	0.274	0.262	0.321	0.206
$n = 2$	0.575	0.548	0.524	0.641	0.412

TABLE 1. Frequencies from the two-dimensional computation and the linear theories.

When it comes to predicting parameter values at which the instability sets in, the theory of Davies & Carpenter (1997*b*) is not so successful. Critical conditions are those for which r (equation (21)) is zero: i.e. instability is predicted for

$$T \leqslant \frac{1 + 12m}{10(1 + 2m)} \tag{23}$$

which increases from 0.1 to 0.6 as m ranges from zero to infinity. Thus the critical value of T indeed increases as m increases, as found numerically, but the values given by equation (23) are far lower than the critical values from the numerical solution. This is also consistent with the numerical Orr–Sommerfield solutions of Davies & Carpenter (1997*b*) and of Green & Ellen (1972), from which the critical Reynolds number for either travelling-wave flutter or divergence is above 5000.

Another relevant theory is that of LaRose & Grotberg (1997), who also examined instabilities of developing or fully developed flow in an infinite channel between compliant walls. Their results are not quantitatively comparable with ours because their fairly general model of wall elasticity does not include the case of pure membrane tension. However, they did find (*a*) a long-wave instability involving wall elasticity but independent of wall mass, and (*b*) a flutter instability that arises at a lower flow speed than (*a*) when m is large enough. These results are qualitatively consistent with both Davies & Carpenter (1997*b*) and our findings.

Too much weight should not be placed on the above comparisons because of the approximate nature of the models: even the results of Davies & Carpenter (1997*b*) are for long-wavelength disturbances, on infinite compliant boundaries, constrained to have zero displacement at $x = 0$ and L, and planar when undisturbed. It would be better to solve a finite-membrane model, as did Shayo & Ellen (1974) for a circular pipe. Moreover the different apparent wavenumber for wall displacement and for pressure, given by the full computations, emphasizes the nonlinear character of the real system.

Energy dissipation

As the rate of energy dissipation in the flow domain is believed to play an important role in the mechanism of the oscillations for a massless membrane, it is of interest to see how the energy dissipation is changed from that case. We investigate this at a time when the flutter-type oscillations have just appeared but not yet become dominant, since there is no doubt that as the wall motions change dramatically at a later stage, the energy dissipation would change accordingly. Investigating the distribution of the energy dissipation at an early stage may help us to see what is the driving force for flutter to appear.

The darker curves in figures 10–12 are the contours of the rate of viscous energy dissipation per unit volume, $\Phi = (u_{i,j} + u_{j,i})^2/2Re$, calculated at each point in the flow domain at a number of times throughout the computation for the Cases I, II and III. The lighter contours underneath are the corresponding streamlines.

It is clear that as in the case without wall inertia (Luo & Pedley 1996) the principal energy dissipation sites are located in the thin boundary layers on the two channel walls in the neighbourhood of and upstream of the narrowest point, as well as in various places downstream: in the shear layer at the edge of the primary separation zone and on the channel walls near the crests and troughs of the vorticity wave. The contributions from each part of the flow domain can be estimated by integrating Φ over four different sections of the channel (with x in the ranges 5–9, 9–13, 13–17, 17–21) together with the total dissipation rate (5–21), as shown in figure 16(a, b, c) for all the three cases. Again, the solid lines are for $m = 0.1$, and the dashed lines are those with $m = 0$. The first section corresponds roughly to the zone upstream of the narrowest point, the second to the shear layer bounding the primary separation region, and the third and fourth to zones affected only by the vorticity waves.

It seems that, apart from some small phase changes, wall inertia does not change the contribution of each section significantly. As before, for the gentle slow mode oscillations, in Cases I and II, it is still the upstream section up to the narrowest point, i.e. curve 1 in figure 16, which dissipates the largest proportion of the energy. The immediate downstream section, including the primary flow separation zone, represented by curve 2, comes second. Less energy is dissipated further downstream (curves 3 and 4). More precise interpretation is harder because of the (small) longitudinal motion of the constriction. Only when the oscillation becomes more violent and highly nonlinear, as in Case III, does the the second section (curve 2), i.e. the primary flow separation region, dissipate significantly more energy during part of the cycle (figure 16*c*). In general, the main features of the energy dissipation integrals remain the same as in cases without wall inertia, at least before the flutter becomes very strong. This implies that it is not a change in the energy dissipation in the different sections of the flow field that enhances the growth of the flutter.

Energy transfer to the wall.

One common feature in the instabilities induced by wall inertia is that all the oscillations are growing waves, and they grow more rapidly than the tension-induced oscillations. This means that there must be a way for the system to transfer energy continuously to the membrane, which in turn is converted into oscillation.

There is indeed a phase difference between the wall pressure and wall displacement during the flutter, which enables the fluid to do work on the wall (Miles 1957; Benjamin 1963; Carpenter & Garrad 1986; Carpenter & Morris 1990). Thus there is the possibility of a destabilizing energy transfer to the wall. To see how much work is done by the fluid on the wall, we calculated the term $p_w v_w$ over some time period, say, $t = 21.38$–34.23 for Case IV (figure 14), and it is plotted against x_w along the elastic section in figure 17. It seems that this work is positive for some parts of the membrane and negative for other parts. However, the overall sum of the energy transfer remains positive, being about 0.4722 for this case. In other words, during this time period there has been a net transfer of 0.4772 units of energy into the wall, which is about 25% of the average total energy dissipation over the same time period in the whole flow field. Obviously, it is this energy transfer that makes the flutter grow.

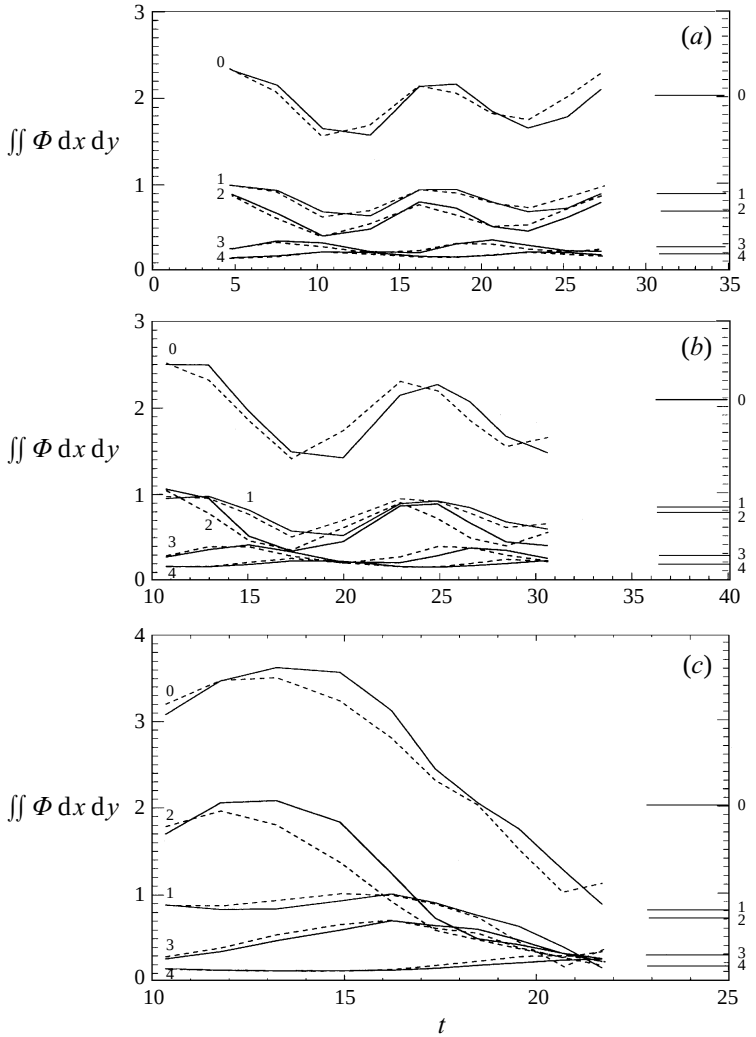

FIGURE 16. Volume integrals of dissipation rate Φ over the whole channel and over four subsections $\int_0^{y_w} \int_a^b \Phi dx dy$: curve 0: $a = 5$, $b = 21$ (whole channel); curve 1: $a = 5$ $b = 9$; curve 2: $a = 9$, $b = 13$, curve 3: $a = 13$, $b = 17$, curve 4: $a = 17$, $b = 21$. (*a*) Case I, $\beta = 30$; (*b*) Case II, $\beta = 32.5$; (*c*) Case III, $\beta = 35$. Solid lines represent the results for $m = 0.1$ and the dashed lines are the ones with $m = 0$. The dissipation rates for steady flow at the same values of β and *Re* are shown at the right-hand side.

Comparison with experiments

A direct quantitative comparison of the present model with experiment is not possible because approximately two-dimensional channels do not occur naturally and have not (yet) been constructed experimentally. There have, however, been many experiments on collapsible tubes, and we have already confirmed that some features of the low-frequency oscillations found numerically are qualitatively similar to those observed experimentally (Luo & Pedley 1996). Experimental studies in which high-frequency oscillations are observed, sometimes superimposed on lower-frequency oscillations, include those of Weaver & Paidoussis (1977), Webster *et al.* (1985), Sakurai & Ohba (1986), Bertram (1986), Gavriely *et al.* (1989) and Bertram *et al.* (1990, 1991). The

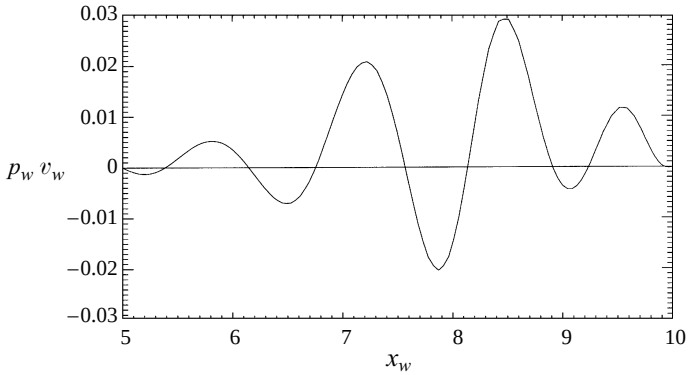

FIGURE 17. The work done by the fluid on the elastic wall: average value of $p_w v_w$ over the time period $t = 21.38$–34.23 for Case IV, $\beta = 25$, and $m = 0.1$, plotted along the wall.

studies of Bertram and his colleagues involved water flow in thick-walled tubes, so both the effective value of m would be relatively large and the elastic properties of the tube would have been very different from those assumed in this paper. No doubt some of Bertram's high-frequency oscillations can be attributed to flutter, stemming from wall mass, but comparison with the present model would be meaningless. Wall mass would have been even more dominant in the experiments of Gavriely *et al.* (1989) who studied airflow in a thick-walled tube; they found, nevertheless, that there was reasonable agreement with a two-dimensional flutter model, in which the bending stiffness of the wall was more important than longitudinal tension. Webster *et al.* (1985) studied airflow in a 'mechanical trachea', consisting of a tube with square cross-section (when undeformed), one side of which was replaced with a membrane under biaxial tension; when deformed, this system is not approximately two-dimensional nor tube-like. Weaver & Paidoussis (1977) studied the stability of thin-walled tubes conveying water, and reported a flapping-mode flutter and classical shell-mode flutter depending on the initial collapsed states of the tubes. They found that the finite-length, standing wave model best described the flapping-mode flutter which has relatively smaller amplitude and occurs mostly for initially collapsed tubes. Perhaps the experiment most relevant to the present analysis was that of Sakurai & Ohba (1986), who studied airflow through a very thin-walled Penrose tube. They reported that self-excited oscillations took place, for a wide range of flow conditions, and were similar to those observed with water flow. At certain flow conditions, however, a strong 'resonant oscillation', accompanied by a sharp sound took place and they observed that the frequency of the resonant oscillation was 4 or 5 times higher than that of the ordinary oscillation (Sakurai & Ohba 1986). No such 'resonant oscillation' has been reported from experiments with water flow, to the best of our knowledge, implying that it was a caused by the higher wall mass ratio. The observed frequency was also comparable with our prediction, for which flutter frequencies are about 4–8 times the original mode frequencies (see Cases I–III).

Flow limitation

As mentioned in the introduction, it would be of interest to use the opportunity provided by our complete numerical solution to investigate whether there is a causal link between the onset of flutter or other oscillations and the occurrence of flow limitation. In a finite-length collapsible tube, flow limitation is seen as the (steady)

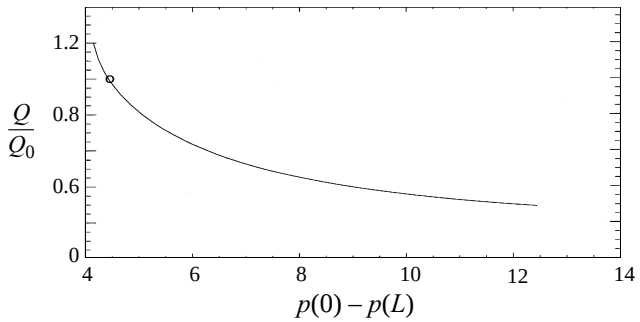

FIGURE 18. The flow-rate rate Q/Q_0(where Q_0 is the flow-rate corresponding to $Re = 200$) plotted against the pressure drop $p(0) - p(L)$.

driving pressure difference along the collapsible segment, $\overline{p}(0) - \overline{p}(L)$, is increased while the transmural pressure at the upstream end, $\overline{p}(0) - \overline{p}_e$, is held constant. For small driving pressures the flow rate $\overline{Q}$ increases, but once the downstream transmural pressure, $\overline{p}(L) - \overline{p}_e$, becomes negative, collapse begins at the downstream end and the flow rate becomes constant (see Grotberg 1994). According to one-dimensional models, flow limitation is associated with a 'choking' phenomenon, by which the fluid velocity cannot exceed the local propagation speed of long, infinitesimal, area waves.

To investigate flow limitation in our two-dimensional model, it is necessary to conduct steady flow computations with the pressure given at the upstream end of the system as well as at the downstream end, and to regard the flow rate as unknown. This leads to a set of new boundary conditions upstream and downstream. The computation is also complicated by the fact that our non-dimensionalization (5) involves the upstream average velocity U_0 in the scales for pressure and tension. However, starting from one of the steady flows already computed, and whose stability has been examined by the methods of this and the preceding paper (Luo & Pedley 1996), we can fix the velocity scale U_0 for that case, thereby fixing Re, T and $p(0) - p_e$, and then compute the actual flow for various neighbouring values of the upstream pressure $p(0)$.

Unfortunately, this system appears to be numerically highly unstable compared with the previous one where flow rate is prescribed upstream. Computing flows for the same conditions, i.e. $Re = 300$, proved impossible even with carefully chosen initial conditions and a relaxation factor as small as 0.1. It is worth pointing out that this may not be a purely numerical difficulty, but that the system with fixed upstream pressure may be intrinsically more complex and unstable than that with fixed upstream flow rate. Such increased complexity was found even in a grossly oversimplified lumped parameter model, because the governing ordinary differential equation was third order rather than second order (Bertram & Pedley 1982).

A complete survey of instabilities and their relation to flow limitation will require a new numerical approach. However, we have studied one case which starts with a lower Reynolds number for which we could achieve convergence using the current code. The case chosen has $Re = 200$, $T = 178.916/\beta$, $\beta = 30$, $p_e - p_d = 3.73$, for which $p(0) - p_e = 0.714$. The results, in the form of a graph of ratio of steady flow rate Q to the initial flow rate Q_0 (corresponding to $Re = 200$) versus $p(0) - p(L)$ is shown in figure 18; flow limitation is indeed observed in that Q decreases as the pressure drop increases. In addition to computing the steady flow, we have also used the unsteady code of the present paper (with Q fixed $= Q_0$) to investigate the stability

of the steady state for different values of m. The steady flow was found to be stable for the massless membrane (Luo & Pedley 1996). The new computations show that the system is stable when $m \leqslant 0.2$, whereas self-excited oscillations set in for $m \geqslant 0.3$. The results for smaller m show that the occurrence of flow limitation is not a sufficient condition for self-excited oscillations when the inflow rate is fixed, but further study is clearly required.

6. Conclusion

Effects of different values of mass ratio m on the flow in a two-dimensional collapsible channel have been studied. It was found that for $m = 0.01$, a value relevant to blood flow in arteries and veins, or experiments with water as the fluid, wall inertia has a negligible effect on the self-excited oscillations. This implies that for this type of system, tension-induced instabilities are the main cause of the self-excited oscillations. For $m = 0.1$, a value more relevant to air flow in the lung, or experiments with air as fluid, flutter-type oscillations are found to develop and play an important role in destabilizing the system. The common feature of the flutter that is different from the original oscillations is that they are all growing waves, transferring energy from the fluid to the wall. The presence of wall inertia (with $m = 0.1$) also increases the critical value of the tension below which the system becomes unstable. Energy dissipation integrals from different parts of the flow domain are found not to change prior to the flutter, implying that this is not the main driving mechanism. As the mass ratio is further increased, the flutter frequency is found to fall, but a large exponential growth in the amplitude of the wall wave soon makes the numerical scheme break down. Neither flutter nor the oscillations previously found are well-correlated with the occurrence of flow limitation.

Much of this work was performed when both authors were in the Department of Applied Mathematical Studies, University of Leeds. We are grateful to the University of Leeds Academic Development Fund and to the SERC (now EPSRC), grant No. GR/G39174, for financial support of this work. Special thanks are due to Dr C. Davies and Dr C. Morfey for helpful discussions.

REFERENCES

Acheson, D. J. 1990 *Elementary fluid dynamics*, Chap. 4. Oxford University Press

Benjamin, T. B. 1963 The threefold classification of unstable disturbances in flexible surfaces bounding inviscid flows. *J. Fluid Mech.* **16**, 436–450.

Bertram, C. D. 1982 Two modes of instability in a thick-walled collapsible tube conveying a flow. *J. Biomech.* **15**, 223–224.

Bertram, C. D. 1986 Unstable equilibrium behaviour in collapsible tubes. *J. Biomech.* **19**, 61–69.

Bertram, C. D. & Pedley, T. J. 1982 A mathematical model of unsteady collapsible tube behaviour. *J. Biomech.* **15**, 39–50.

Bertram, C. D., Raymond, C. J. & Pedley, T. J. 1990 Mapping of instabilities for flow through collapsed tubes of different length. *J. Fluids Struct.* **4**, 125–154.

Bertram, C. D., Raymond, C. J. & Pedley, T. J. 1991 Application of nonlinear dynamics concepts to the analysis of self-excited oscillations of a collapsible tube conveying a fluid. *J. Fluids Struct.* **5**, 391–426.

Bonis, M. & Ribreau, C. 1978 Etude de quelques propriétés de l'écoulement dans une conduite collabable. *La Houille Blanche* **3/4**, 165–173.

Brower, R. W. & Scholten, C. 1975 Experimental evidence on the mechanism for the instability of flow in collapsible vessels. *Trans. ASME: J. Biomech. Engng.* **13**, 389–845.

Cancelli, C. & Pedley, T. J. 1985 A separated-flow model for collapsible-tube oscillations. *J. Fluid Mech.* **157**, 375–404.

Carpenter, P. W. & Garrad, A. D. 1986 The hydrodynamic stability of flow over Kramer-Type compliant surfaces. Part 2. Flow-induced surface instabilities. *J. Fluid Mech.* **170**, 199–232.

Carpenter, P. W. & Morris P. J. 1990 The effect of anisotropic wall compliance on boundary-layer stability and transition. *J. Fluid Mech.* **218**, 171–223.

Conrad, W. A. 1969 Pressure-flow relationships in collapsible tubes. *IEEE Trans. Bio-Med. Engng* **16**, 284–295.

Davies, C. 1995 Evolution of Tollmien-Schlichting waves over a compliant panel. Ph.D thesis, University of Warwick.

Davies, C. & Carpenter, P. W. 1997*a* Numerical simulation of the evolution of Tollmien-Schlichting waves over finite compliant panels. *J. Fluid Mech.* **335**, 361–392.

Davies, C. & Carpenter, P. W. 1997*b* Instabilities in a plane channel flow between compliant walls. *J. Fluid Mech.* **352**, 205–243.

Gavriely, N. & Grotberg, J. B. 1988 Flow-limitation and wheezes in a constant flow and volume lung preparation. *J. Appl. Physiol.* **64**, 17–20.

Gavriely, N., Shee, T. R., Cugell, D. W. & Grotberg, J. B. 1989 Flutter in flow-limited collapsible tubes: a mechanism for generation of wheezes. *J. Appl. Physiol.* **66**, 2251–2261.

Green, C. H. & Ellen, C. H. 1972 The stability of plane Poiseuille flow between flexible walls. *J. Fluid Mech.* **51**, 403–416.

Gresho, P. M., Lee, R. L. & Sani, R. L. 1979 On the time-dependent solutions of the Navier–Stokes equations in two and three dimensions. In *Recent Advances in Numerical Methods in Fluids* (ed. C. Taylor & K. Morgan), vol. 1, pp. 27–79.

Grotberg, J. B. 1994 Pulmonary flow and transport phenonmena. *Ann. Rev. Fluid. Mech.* **26**, 529–571.

Grotberg, J. B. & Gavriely, N. 1989 Flutter in collapsible tubes: a theoretical model of wheezes. *J. Appl. Physiol.* **66**, 2262–2273.

Grotberg, J. B. & Reiss, E. L. 1984 Subsonic flapping flutter. *J. Sound Vib.* **92**, 349–361.

Grotberg, J. B. & Shee, T. R. 1985 Compressible-flow channel flutter *J. Fluid Mech.* **159**, 175–193.

Heisenberg, W. 1924 Uber Stabilität und turbulenz von flussigkeitsströmen. *Ann. Phys. Leipzig* **74**, 577–627.

Jensen, O. E. 1990 Instabilities of flow in a collapsed tube. *J. Fluid Mech.* **220**, 623–659.

Jensen, O. E. 1992 Chaotic oscillations in a simple collapsible tube model. *Trans. ASME: J. Biomech. Engng.* **114**, 55–59.

Jensen, O. E. & Pedley, T. J. 1989 The existence of steady flow in a collapsed tube. *J. Fluid. Mech.* **206**, 339–374.

Kamm, R. D. & Pedley, T. J. 1989 Flow in collapsible tubes: a brief review. *Trans. ASME*: *J. Biomech. Engng.* **111**, 177–179.

LaRose P. G. & Grotberg, J. B. 1997 Flutter and long-wave instabilities in compliant channels conveying developing flows. *J. Fluid. Mech.* **331**, 37–58.

Lowe, T. W., Luo, X. Y. & Rast, M. P. 1996 A comparison of three solution methods for flow in a collapsible channel. Preprint.

Lowe, T. W. & Pedley, T. J. 1995 Computation of Stokes flow in a channel with a collapsible segment. *J. Fluids Struct.* **9**, 885–905.

Lucey, A. D. & Carpenter, P. W. 1992 A numerical simulation of the interaction of a compliant wall and inviscid flow. *J. Fluid Mech.* **234**, 147–170.

Luo, X. Y. & Pedley, T. J. 1995 Numerical simulation of steady flow in a two-dimensional collapsible channel. *J. Fluids Struct.* **9**, 149–197.

Luo, X. Y. & Pedley, T. J. 1996 Numerical simulation of unsteady flow in a two-dimensional collapsible channel. *J. Fluid Mech.* **314**, 191–225, and corrigendum, **324**, 408–409.

Matsuzaki, Y. & Matsumoto, T. 1989 Flow in a two-dimensional collapsible channel with rigid inlet and outlet. *Trans. ASME*: *J. Biomech. Engng* **111**, 180–184.

Miles, J. W. 1957 On the generation of surface waves by shear flow. *J. Fluid Mech.* **3**, 185–199.

Ohba, K., Yoneyama, N., Shimanaka, Y. & Maeda, H. 1984 Self-excited oscillation of flow in collapsible tube, I. *Tech. Rep. Kansai University* **25**, 1–13.

Pedley, T. J. 1992 Longitudinal tension variation in a collapsible channel: a new mechanism for the breakdown of steady flow. *Trans. ASME*: *J. Biomech. Engng*. **114**, 60–67.

Pedley, T. J. & Stephanoff, K. D. 1985 Flow along a channel with a time-dependent indentation in one wall: the generation of vorticity waves. *J. Fluid Mech.* **160**, 337–367.

Rast, M. P. 1994 Simultaneous solution of the Navier–Stokes and elastic membrane equations by a finite-element method. *Intl J. Numer. Meth. Fluids* **19**, 1115–1135.

Reyn, J. W. 1974 On the mechanism of self-excited oscillations in the flow through collapsible tubes. *Delft Progress Rep.* **1**, 51–67.

Ruschak, K. J. 1980 A method for incorporating free boundaries with surface tension in finite element fluid-flow simulators. *Intl J. Numer. Meth. Engng* **15**, 639–648.

Sakurai, A. & Ohba, K. 1986 Self-excited oscillation of flow in collapsible tube. III. *Tech. Rep. Kansai University* **27**, 41–48.

Saito, H. & Scriven, L. E. 1981 Studying of coating flow by the finite element method. *J. Comput. Phys.* **42**, 53–76.

Shapiro, A. H. 1977 Steady flow in collapsible tubes. *Trans. ASME: J. Biomech. Engng* **99** 126–147.

Shayo, L. K. & Ellen, C. H. 1974 The stability of finite length circular cross-section pipes conveying inviscid fluid. *J. Sound Vib.* **37**, 535–545.

Silliman, W. J. 1979 Viscous film flows with contact lines. PhD Thesis, University of Minnesota.

Tutty, O. R. & Pedley, T. J. 1993 Oscillatory flow in a stepped channel. *J. Fluid Mech.* **247**, 179–204.

Weaver, D. S. & Paidoussis, M. P. 1977 On collapse and flutter phenomena in thin tubes conveying fluid. *J. Sound Vib.* **50**, 117–132.

Webster, P. M., Sawatzky, R. P., Hoffstein, V., Leblanc, R., Hinchey, J. M. & Sullivan, P. A. 1985 Wall motion in expiratory flow limitation: choke and flutter. *J. Appl. Physiol.* **59**, 1304–1312.